Calibrated Electrochemical Impedance Spectroscopy and Time-Domain Measurements of a 7 kWh Automotive Lithium-Ion Battery Module with 396 Cylindrical Cells

Manuel Kasper,[a] Manuel Moertelmaier,[a] Mykolas Ragulskis,[a] Nawfal Al-Zubaidi R-Smith,[a] Johannes Angerer,[b] Mathias Aufreiter,[b] Alberto Romero,[b] Jakob Krummacher,[b] Jianjun Xu,[c] David E. Root,[c] and Ferry Kienberger*[a]

A 7 kWh automotive battery module with 396 interconnected cells was tested with electrochemical impedance spectroscopy (EIS) and time-domain pulsing over 260 charge-discharge cycles. An EIS calibration workflow was developed for low complex impedance values in a frequency range of 1 kHz to 50 mHz. Significant corrections on the resistance and the reactance were obtained from the calibration, particularly at frequencies above 100 Hz. Equivalent circuit parameters were extracted from the EIS spectra and the pulse response and investigated with respect to the cycle number and state-of-charge (SoC). Fit parameters were robustly extracted including R_{sol}, R_{ct}, and L from EIS, and R_0, τ_1 and τ_2 from time-domain pulsing. The ohmic resistance decreased over the cycling number indicating an enhanced wetting of the electrodes. Charge transfer resistance R_{ct} showed a monotonic increase over the cycles related to cell ageing. From the charge and discharge pulses, the ohmic resistance R_0 was determined from the instantaneous voltage step of the recovery pulse, while the two time constants τ_1 and τ_2 correspond to the slower exponential recovery phase. R_0 from the time-domain showed a similar trend as R_{sol} plus a contribution of R_{ct} from EIS. Overall, we show that calibrated EIS and time-domain pulsing are efficient methods to gain insights into the electrochemical processes related to different SoCs and the cycling ageing of battery modules and packs.

Introduction

Battery packs are a key component of electric vehicles (EVs), and the performance and cost of an EV are both heavily dependent upon the battery pack's performance and lifespan.[1] A battery pack is typically constructed by connecting several (1–50) modules in series, with each module containing hundreds of interconnected lithium-ion battery (LiB) cells.[2] Today, the total pack capacity for EVs may contain ranges from 30 kWh to 120 kWh, supporting up to 600 km of EV range per charging cycle.[3] Overall, a high cycling stability is achieved, which is defined by the number of charge-discharge cycles where the actual capacity drops below the nominal capacity to a certain degree, for instance to 80% of the initial value. The state of health (SoH) is such a measure with units given in percentage points of the actual capacity over the nominal capacity. The accurate and reliable characterization and classification of LiBs are therefore crucial for the quality control of battery modules and packs.[4] Thereby, electrical impedance and internal resistance are essential parameters for quantifying SoH, battery performance, energy efficiency, and corresponding ageing mechanisms.[5] For instance, the complex impedance, including the resistance (real part) and the reactance (imaginary part), is correlated to the battery state of charge (SoC) and SoH.[6] As the battery ages, either because of calendar aging or cycling aging, its impedance increases due to the degradation of the electrode materials, electrolyte, and the corrosion of cell connectors, reducing the SoH.

The impedance of LiB cells, modules and packs is typically measured in electrochemical impedance spectroscopy (EIS).[7] In the EIS galvanostatic approach, a sinusoidal current of a certain amplitude and frequency is applied to the battery while measuring the voltage response including amplitude and phase shift.[8] EIS data is collected in a wide frequency range, typically in the mHz to the kHz range, allowing disentangling of different electrochemical processes during battery operation.[9] Due to the small amplitude of the stimulus current, the cell is only marginally moved from its equilibrium potential. Practically, the phase difference between current and voltage and their amplitudes are used to calculate the complex raw impedance at each frequency, which can be visualized in a complex plane

[a] M. Kasper, Dr. M. Moertelmaier, M. Ragulskis, Dr. N. Al-Zubaidi R-Smith,
Dr. F. Kienberger
Keysight Laboratories,
Keysight Technologies Austria GmbH
Linz 4020 (Austria)
E-mail: Ferry_kienberger@keysight.com

[b] J. Angerer, M. Aufreiter, Dr. A. Romero, Dr. J. Krummacher
Kreisel Electric GmbH
Rainbach i.M. 4261 (Austria)

[c] Dr. J. Xu, Dr. D. E. Root
Keysight Laboratories
Keysight Technologies Inc.
Santa Rosa, CA 95403 (USA)

Batteries & Supercaps

Research Article
doi.org/10.1002/batt.202200415

Chemistry Europe
European Chemical
Societies Publishing

with the frequency as an independent parameter and equal axis scaling for the real and imaginary axis (Nyquist plot). Recently, several EIS-based studies have been conducted to investigate LiB cells. For instance, EIS has been used for cell quality evaluation,[10] SoC and SoH estimation,[11] temperature monitoring,[12] as well as electrochemical ageing of cells.[13] So far, EIS studies mostly examined individual cells or low voltage modules, with only a few studies dealing with high voltage battery modules and packs as required for EVs. For example, EIS was employed to detect module degradation in an 11 kWh LiB based on an impedance increase.[14] Additionally, a complete battery pack was characterized using EIS, and its impedance was evaluated depending on its SoC.[4] In practice, the accuracy of EIS measurement is limited by systematic and random errors.[15] It was shown recently that systematic errors can be corrected by specific calibration and correction methods, while random errors can be addressed by employing best measurement practices.[16]

In addition to EIS, which is a frequency-domain measurement, time-domain pulse methods are also applicable to study high voltage battery modules. Pulse methods are faster and more practicable because they require simpler measurement hardware. Typically, pulse response measurements provide parametrization values for equivalent electric circuit models, which in turn can be used to extract certain electrochemical properties of the batteries. The voltage response of a battery during a pulsed current charge or discharge can be divided into two parts, a fast step response and a slow exponential response. The instant voltage drop is caused by the ohmic resistance of the battery, which is related to the solution resistance R_{sol}, the ratio of the electrode area to the pores, and parts of the charge transfer resistance. The slow exponential phase is typically described by an RC component representing the charge transfer kinetics and the slower diffusion process.[17] There are several standard pulse tests to determine the dynamic properties of a battery. For instance, the hybrid pulse power characterization (HPPC) method consists of a discharge current pulse with 10 seconds width and high C-rate followed by a regenerative charge pulse with the same duration and C-rate.[18] Other dynamic pulse cycle profiles for EVs are defined in the literature, such as the world harmonized light vehicle test procedure (WLTP), applicable for determining energy consumption, performance, and the electric range of EVs based on real-world driving cycles.

In this paper, we test an automotive battery module with 7 kWh capacity using EIS and time-domain pulse measurements at different SoCs and 260 charge-discharge cycles. Equivalent Circuit Model (ECM) modeling is used to extract relevant electrochemical cell parameters from both methods. The parameters obtained are analyzed with regards to SoC and the cycling number of the module. An EIS calibration process is developed using short and shunt standards to obtain error coefficients that are used in a correction process allowing for precise measurements of low impedance over a broad frequency range of 10 mHz to 10 kHz. A comparison of frequency and time-domain model parameters is done reveal-

ing trends consistent across methods for varying SoC and cycling number.

Materials and Methods

LiB modules

The 11S36P module consists of 11 blocks in series where each block includes 36 parallel connected cylindrical 21700 cells. Thus, the total number of cells in one module is 396. Each cell has a nominal voltage of 3.7 V and a capacity of 4.9 Ah (18.1 Wh/cell), and the module has a capacity of 176.4 Ah, a voltage of 40.7 V, and an energy rating of 7 kWh. The module is equipped with a battery management system (BMS) which is also used for balancing the cell voltages. The communication to the BMS is established through a CAN (control area network) bus interface. An external 12 V power supply is used to power the BMS.

Module test hardware and setup

Figure 1a shows a schematic of the module test system. It includes a three-phase powered module tester (Keysight SL1001 A) with ratings of up to 100 V and 200 A for voltage and current, respectively. During the discharge phase, the power is fed back to the grid with over 90% efficiency. Separate force and sense connections are used to connect the module to the tester via a four-wire Kelvin connection. The force wires are armed cables of 100 mm² cross-section to keep the joule heat losses (I²R) low. An independent safety supervision system monitors the individual cell voltages, the cell temperatures, the cooling flow rate and the current. In case of any abnormal values the safety supervision system shuts down the test, and the module is disconnected by a high-power switch (80 kA rated service current). Liquid cooling of the module is implemented using an external thermo-chiller (SMC HRS012-AF-20) with a cooling capacity of 2 kW. The coolant trajectory through the module is shown with colored arrows in Figure 1(a). Figure 1(b) shows a photograph of the module and the various connectors, including force and sense wiring and the BMS interface. The module and the connectors are installed inside a safety chamber which ensures fire safety in the unlikely case of a catastrophic battery failure. The electrical connections and the cooling pipes are fed through gas-tight connections from the outside of the chamber, where the test hardware resides, to the inside of the chamber. All BMS related equipment (power supply, CAN interface) installed in the chamber are shown in Figure 1(b).

Module EIS calibration

The sense voltage connection is terminated in a break-out box which has built-in calibration capabilities, ensuring that a defined EIS calibration plane is established (Figure 1b). The box
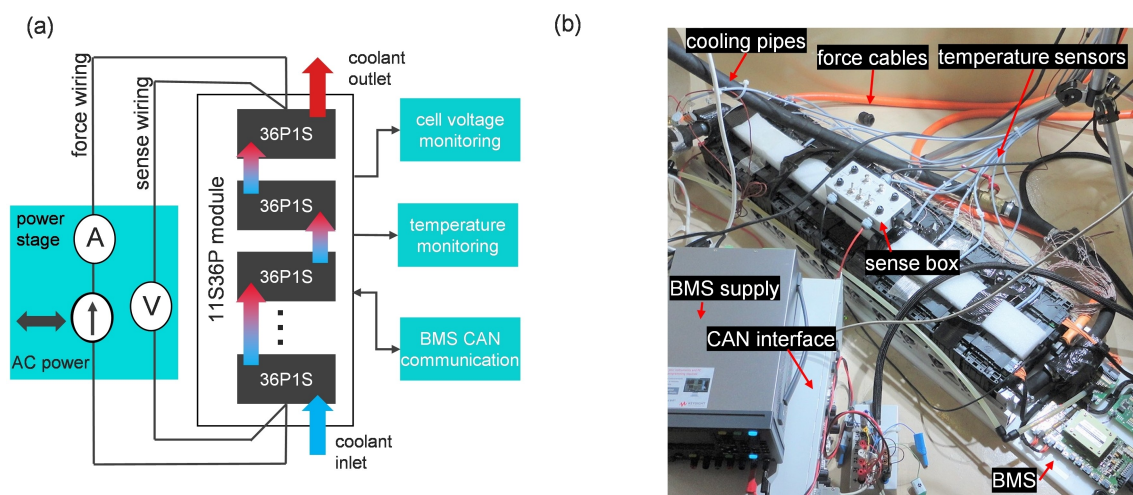
Figure 1. The module test setup. a) Conceptual overview of the test setup with a 4-wire connection to the 11S36P module containing 11 series connected blocks and 36 parallel connected cells per block. The test system includes a three-phase powered tester with discharging power feed back to the grid. The liquid cooling flow is indicated by colored arrows. b) Photograph of the module with the various connections, cooling pipes, temperature sensors, BMS, and interface to the BMS control.

provides connections for the force wires and built-in switches that allow selecting either a built-in short standard or BNC terminals that are connected to the external shunt standard. After the calibration measurements, the force wires are connected to the battery module and the switches are set to a third position which connects the sense wires to the battery module. This procedure allows for a system calibration with a minimum of wire movement resulting in a well-defined calibration plane close to the module. Thereby, the calibration plane is defined by the short sense wires that connect the sense box to the module. Under these conditions, the systematic error introduced by the force wires and the long sense wires between the sense box and tester hardware is therefore not affecting the measurement results. The EIS raw quantities are calibrated using a two-term correction technique.[16] The calibration is performed over a frequency range of 1 kHz to 50 mHz and uses a short standard and a coaxial shunt standard of known resistance value (100 mΩ). There are two components that contribute to the systematic error of the measured impedance (Z_m), a series impedance (Z_{ser}) and a complex gain

(k). The true impedance of the module (Z_t) is obtained by the following relation: $Z_t = (Z_m - Z_{ser})/k$. Furthermore, all temperatures are read by the module tester resulting in coherent temperature readings that are synchronized with the test plan. The inlet temperature is kept constant at 30 °C by the control mechanism of the chiller while the outlet temperature depends on the heat dissipated in the module. Temperature sensors are positioned across the module to determine the temperature spread as well as inside the inlet and the outlet flow.

Test series and measurement workflow

Figure 2(a) provides an overview of the test plan and Figure 2(b) shows the corresponding module excitation current within one cycling sequence. The test sequence is divided into four steps I–IV that are continuously repeated in a loop. In step I, the module is charged to 100 % SoC in a constant current/constant voltage (CC/CV) scheme with a C-rate of 1 C (174 A). The CC charging is switched to CV once a voltage of 4.20 V/cell
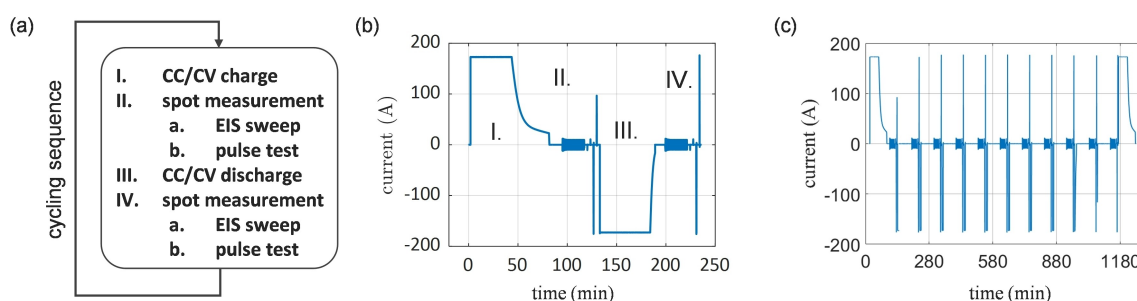

Figure 2. Test series and measurement workflow. a) Cycling sequence including the four steps in each cycle. b) Excitation current profile for one cycle showing the four steps that are continuously repeated: (I) CC/CV charge, (II) EIS and pulse spot measurements (shown at 100 % SoC), (III) CC/CV discharge, and (IV) EIS and pulse spot measurements. c) Excitation current profile for the extended test cycle applied at every 10th charge-discharge cycle. The extended test cycle includes steps I–IV with partial discharge steps of 10 % SoC, from 100 % to 0 % SoC.

Batteries & Supercaps

Research Article
doi.org/10.1002/batt.202200415

Chemistry
Europe
European Chemical
Societies Publishing

is reached (corresponding to 46.2 V for the module). The CV mode is used to charge the module to 100% SoC, and once the current falls below the cut-off threshold of C/10 (17.4 A) the CV period is terminated. The total charge time is about 80 minutes followed by a 15-minute rest period. After each charging step the imbalance of the 11 individual block voltages is checked. If a threshold of 20 mV is exceeded a passive balancing process with a current of 100 mA/block is initiated. Once the imbalance has decreased below 5 mV the balancing process is stopped, and the test plan is continued.

In step II, various spot measurements are done at 100% SoC, including EIS sweeps and pulse tests. Calibrated EIS is performed, with frequencies being swept from 1 kHz to 50 mHz over 50 logarithmically distributed points. The excitation current for the module is 10 A_{pk}, corresponding to 278 mA_{pk} per cell (± 10 mA). Additionally, a time domain pulse test is performed at two different current amplitudes (10 A and 174 A). Each pulse is 10 seconds wide followed by a 10-minute relaxation period. Each pulse amplitude is measured at both polarities in order to keep the excitation sequence average-free and to identify if there are differences in the response based on the polarity. The two different current amplitudes allow for an analysis of the voltage response with respect to the current. The smaller 10 A current is well within the small-signal region while the 174 A current (corresponding to 1 C) has a larger signal-to-noise ratio (SNR). It should be noted that at 100% SoC the positive pulse test is limited to about 98 A, due to the upper voltage limit of the module tester, as shown in Figure 2(b), step II.b. The total measurement time for the EIS and pulse test is about 40 minutes. In step III the module is discharged to 0% SoC in a CC/CV procedure analogous to the charging procedure with a cut-off current of C/10. The C-rate is again 1 C and the CC mode is switched to CV once the threshold voltage of 3 V/cell (33 V for the module) has been reached. In the CV period, the voltage is kept constant at 3 V/cell until the current decreases below the cut-off current of C/10 (17.4 A). The discharge time is about 60 minutes. In step IV, the spot measurements are repeated at 0% SoC. The complete cycle including steps I–IV takes about 240 minutes, which results in a throughput of 6 cycles/day and 42 cycles/week. In addition, at every 10th cycle, an extended test cycle is done, as shown by the current profile in Figure 1c. This includes performing steps (I–IV) at 10% discharge steps covering the range of SoC from 100% to 0%. A rest period of 60 min is applied after each discharge step. In this study, 260 cycles have been performed in roughly 1.5 months of active measurement time.

Equivalent electric circuit model

For fitting the EIS curve, an equivalent electric circuit model (ECM) topology is defined according to the electrochemical processes occurring in the LiB cells also considering the module setup and module geometry. The ECM includes an inductive element L for the high-frequency behavior, which is particularly sensitive to the cabling and module geometry, a series

resistance representing the solution resistance of the module (R_{sol}), and a ZARC element consisting of a resistor parallel to a constant phase element (CPE) corresponding to the Lithium-ion charge transfer resistance (R_{ct}) and equivalent double layer capacitance (Q_{dl}), ($Q_{dl} || R_{ct}$). The impedance of a ZARC is obtained based on the following relation,[19]

$$ZARC = R/(1 + (j\omega/\omega_c)^{\alpha}), \tag{1}$$

where R is the resistance, j is the imaginary unit, ω is the angular frequency, ω_c is the frequency where the imaginary part is maximum, and α is the fractional order. The double layer capacitance C_{dl} can be related to the effective capacitance Q_{dl} in the ZARC by: $C_{dl} = Q^{1/\alpha} R^{(1-\alpha)/\alpha}$.[9] Finally, a Warburg element (Z_W) describes the liquid and solid phase diffusion of Li$^+$ ions in the active material particles. For real cell data, a series connection of the ZARC element with the Warburg impedance has been shown to be practicable as it leads to good agreement with the Randles model.[20] Based on this model and electrochemical processes the impedance of the module (Z_{Mod}) is defined as:

$$Z_{Mod} = [1/(j\omega L)] + R_{sol} + [R_{ct}/(1 + (j\omega/\omega_c)^{\alpha})] + Z_W \tag{2}$$

The ECM is fit to EIS curves in a semi-automated multi-step procedure. In the first step, high- and low-frequency signals are processed separately to estimate the magnitude of inductive and diffusive contributions. These starting values are then used to initialize a fit of the full model, with parameters being checked in several ways in a final step for optimal fit results. An example of such a check is a heuristic based on experience that demands a restart of the fit if the fitted values for R_{sol} and R_{ct} are outside of the range of measured raw data. It is notable that as local variations are higher at low SoCs, we used EIS acquired at higher SoCs (e.g., 80% SoC) for consistent ECM parameter extraction.

The time domain pulse data is represented by a modified ECM consisting of the resistance R_0 defined by the instantaneous voltage step and a slower bi-exponential phase corresponding to two RC elements ($R_{p1} || C_{p1}$; $R_{p2} || C_{p2}$) in series. The bi-exponential recovery phase can be modeled as:

$$U(t) = U_{OCV} + R_{p1}I\, e^{\frac{-t}{R_{p1}C_{p1}}} + R_{p2}I\, e^{\frac{-t}{R_{p2}C_{p2}}}, \tag{3}$$

where U_{OCV} is the open circuit voltage of the module and I is the amplitude of the current pulse; R_{p1} and C_{p1} are from the fast time constant (τ_1) due to charge transfer process around 1 second, and R_{p2} and C_{p2} are related to the slower time constant (τ_2) due to slow diffusion processes, typically at tens of seconds.

Results and Discussion

For accurate module tests, a dedicated test system was set up, consisting of a three-phase powered module tester with

Batteries & Supercaps

Research Article
doi.org/10.1002/batt.202200415

Chemistry Europe
European Chemical
Societies Publishing

discharge power capabilities to the grid, a BMS with comprehensive temperature and safety features, and a calibration box for EIS and time-domain measurements. Figure 3 shows the calibration procedure and the comparison of calibrated EIS with uncalibrated raw data. In the EIS error model (Figure 3a), an ideal impedance meter is combined with a series error-term Z_{ser} and a complex gain error-term k. The measured impedance Z_m is related to the true impedance Z_t through the complex gain factor k and the offset Z_{ser} by the relation $Z_t = (Z_m - Z_{ser})/k$. Accordingly, two calibration measurements are required to solve the calibration equation system. The calibration measurements were done with a short standard and a 100 mΩ coaxial shunt standard (see the methods section). The electronic channel noise has only a small contribution of around 50 μΩ. Figure 3(b) shows a comparison of the uncalibrated (i.e., original measurement) and the calibrated module impedances in the Nyquist plot in a frequency range of 1 kHz–50 mHz. The comparison test of the raw and calibrated data was conducted at cycle 0, prior to the measurement test plan (Figure 2), and the module was set to 50% SoC. The calibration leads to a significant difference in the EIS data, specifically at frequencies starting around 100 Hz. The higher the frequency the more distorted is the original measurement because of the inductive coupling between force and sense wiring. The same effects were also observed in the EIS spectra of single cells, however, the distortion between raw and calibrated measurements for single cells starts at higher frequencies of 1–3 kHz. The reason is that the module is physically larger with greater cable lengths. Comparing the module resistance to the resistance of single cells, for example at a medium SoC of 50%, the module exhibits a resistance of $R_{Mod} = 6.2$ mΩ at 1 kHz (Figure 3b), while single cells of similar capacity (~5 Ah), chemistry (cathode NMC) and form-factor (cylindrical type 21700) show a resistance of R_{Cell} ~15 mΩ at 1 kHz.[21] Taking into consideration the module configuration 11S36P, good agreement is found with the single cell resistance multiplied by the series number of connected cells ($N_s = 11$) and divided by the parallel number of connected blocks ($N_p = 36$), $R_{Mod} = (R_{Cell} \cdot N_S)/N_P$. The discrepancies observed between the actual cell resistance and the value

calculated are attributable to resistive elements used to protect the cells and connect the blocks electrically in series.

The module was charged and discharged 260 times, and in each cycle of charging and discharging a spot measurement was performed including calibrated EIS sweeps and time-domain pulsing (see the methods section). Each cycle consisted of four steps, starting with a CC/CV charge, followed by EIS and pulse spot measurements, a CC/CV discharge, and finally again EIS and pulse spot measurements. As such, the spot measurements (EIS and pulsing) were done for varying cycling numbers (cycling # 1 to cycling # 260) and at different SoCs (0% SoC to 100% SoC). Figure 4(a) shows the calibrated EIS data at a given cycle number with respect to the SoC between 20% and 80%. While there is no monotonic trend of the impedance with respect to the SoC over the full 0–100% SoC range, higher impedance values are typically observed at low SoCs (around 20% SoC) and lower impedance values are observed at high SoCs (around 80% SoC). Similar trends were observed in previous studies on single LIB.[22] The ohmic resistance values at the end of the first semicircle, representing the sum of the bulk resistances R_{sol} and R_{ct}, are indicated in Figure 4(a) with arrows at 20% SoC (high resistance), 40% SoC (medium resistance), and 80% SoC (low resistance). The charge transfer resistance becomes higher at both ends of the SoC in contrast to intermediate ranges of SoC.[23] The increased resistance at low SoCs is mainly caused by the low-rate extraction of Li$^+$ ions from the graphite anode at low stoichiometries and structural changes at the cathode related to the accommodation of these charges.[24] The ECM [Figure 4b; Equation (2)] was then fit to the calibrated impedance spectra and electrochemical model parameters were extracted (Figure 4c). Two EIS curves and their ECM fits are shown for different cycling numbers and SoCs. The solution resistance R_{sol} describes the ohmic resistance of the electrolyte, the ratio of the electrode surface area and the distance between the electrodes, which can be also described as the separator thickness, and the electrical connectors and is identified by the point where the impedance spectrum crosses the real axis. The charge transfer resistance R_{ct} describes the charge transfer and mass transport of Li$^+$ ions in solid particles
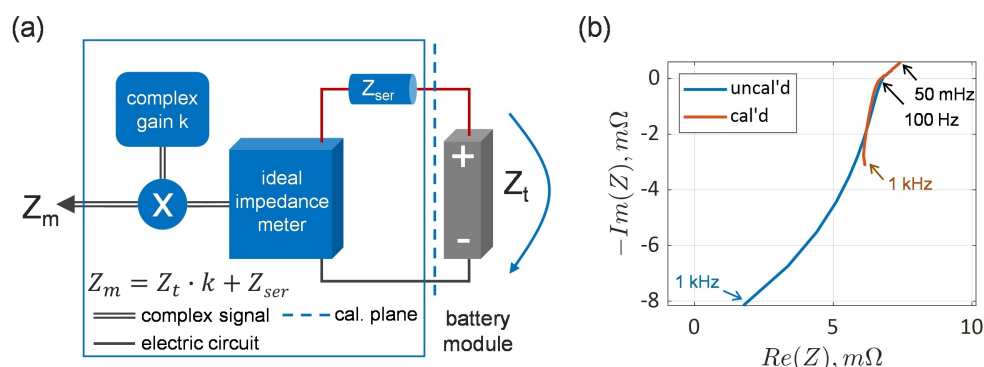

Figure 3. EIS module calibration. a) Error model and workflow for the module test system. The EIS measurement is described by combining an ideal impedance meter with a series error impedance Z_{ser} and a gain error term k. The measured impedance Z_m is related to the true impedance Z_t via the complex gain factor k and the offset Z_{ser}. b) Comparison of raw and calibrated EIS across the frequency range of 1 kHz to 50 mHz. The raw data (blue) and the corrected data (red) are shown for the 7 kWh module measured at room temperature and approximately 50% SoC. Characteristic frequency points are indicated by arrows.
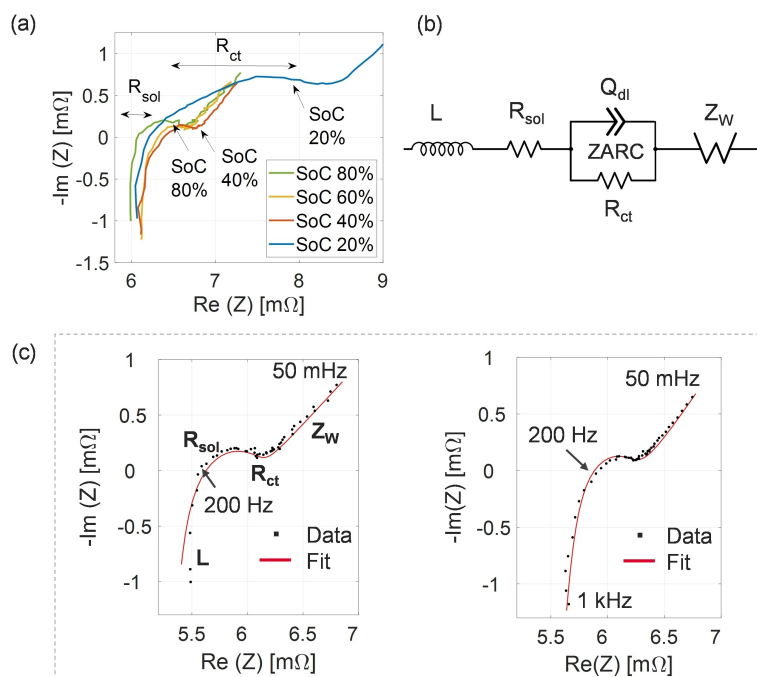
Figure 4. EIS module data and equivalent electric circuit model (ECM). a) EIS spectra superposition at cycle # 99 and varying SoC from 80% to 20%, in a discharge direction. The arrows indicate the ohmic resistance values to the end of the Nyquist semicircle for 20% SoC (blue curve). b) The ECM used to fit the module EIS data. c) Two different EIS spectra fitted with the ECM (left: 80% SoC and cycle # 99; right: 40% SoC and cycle # 69). The minimum and maximum frequency points are labelled (c, right), as well as the point of intersection with the real axis at 200 Hz.

and liquid electrolyte, and it is typically observed at the end of the first semicircle. The double layer capacitance C_{dl} describes the accumulation of charge carriers of opposite signs at the electrode-electrolyte interface, as well as pseudo-capacitance due to absorption/desorption processes or fast Faradic surface reactions.[25] The charge transfer and double layer capacitance are represented by the depressed semicircle (ZARC, a parallel connection of a constant phase element and the charge transfer resistance). Recent work has shown that at higher cycle numbers, EIS spectra start to show two distinct semicircles at intermediate frequencies. This is typically an indication of ageing, such as increased interface layer resistance, dendrite formation and electrode degradation.[26] However, this was not observed in our study over 260 cycles, as the cells were in relatively good SoH. The Warburg impedance Z_w is related to diffusion and mass transport and is represented by the linear slope at low frequencies. The model does not account for the ionic resistance R_{ion}, as it treats the electrode as a homogeneous system.[7] It is notable that an equivalent circuit with two ZARCs would be a more accurate reflection of the electrochemical processes in the cell and the ageing of electrodes. However, in the observed raw data, only a single semicircle is clearly resolvable, especially at SoCs above 0.2. A model with a single ZARC can be used to robustly fit all SoCs.[27]

The values for R_{sol}, R_{ct}, and the inductance L are given in Figure 5 with respect to the cycling number, ranging from cycling # 1 to # 260. Overall, the EIS curves and the ECM fit parameters show a smooth variation with respect to the cycle number and the parameters are extracted robustly (Figure 5a). R_{sol} starts at 6 mΩ and shows a downward trend because the

module was fabricated with new and unused cells, leading to enhanced wetting of the electrodes when the cells are used the first time (Figure 5b). The unwetted active material causes an underutilization of the electrode capacity.[28] Due to this, a decrease in resistance indicates an increase in the wetted electrode/electrolyte interface.[29] The same effect was also observed on fresh individual cells,[30] R_{ct} starts at 0.6 mΩ and it is the main aging related parameter. A continuous increase of R_{ct} from 0.6 mΩ to 1.2 mΩ at cycle # 260 is observed, which is typically explained by the SEI (solid electrolyte interface) layer growth,[31] and the corresponding decrease in the exchange current density due to changes in porosity and the reduced lithium concentration.[32] Figure 5(d) shows the inductance L at a constant value of 170 nH which is related to the fixture, cables, and geometry of the module, which doesn't change over cycling and therefore no significant trend is observed over the module cycling number.

Figure 6 shows the extraction of ECM parameters from the time-domain pulse response data using Equation (3). After each cycle, a spot measurement is done including an EIS sweep and a pulse test at specific SoC values (Figure 6a). Two current pulses are applied each in the charging and in the discharging domains with a pulse height of 10 A and 174 A, and a pulse duration of 10 s with a 3 min pause between pulses. Because the pulses are applied in both plus and minus polarities, the overall module SoC is not changed by this spot measurement.[17] Figure 6(b) shows the voltage response of the end of the discharge pulse at −174 A and the corresponding ECM fit. The ECM consists of a resistive step-function R_0 covering the instantaneous voltage recovery step at the end of
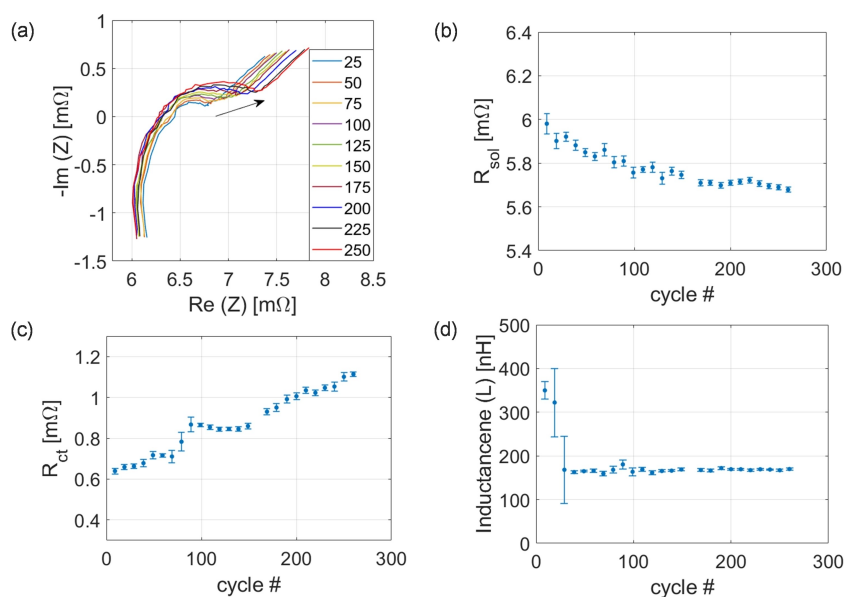
Batteries & Supercaps

Research Article
doi.org/10.1002/batt.202200415

Chemistry Europe
European Chemical
Societies Publishing

Figure 5. ECM parameters extracted from the EIS fit with respect to module cycling number. a) EIS spectra superposition at SoC 100% and varying cycle number ranging from 25 to 250. The arrow indicates increasing R_{ct} values over the cycling number. b–d) The ECM fit parameters are given over the cycling number at 80% SoC: b) solution resistance R_{sol}, c) charge transfer resistance R_{ct}, and d) inductance L. Error bars are shown for the parameters and are computed based on the stability of results across adjacent measurement points.
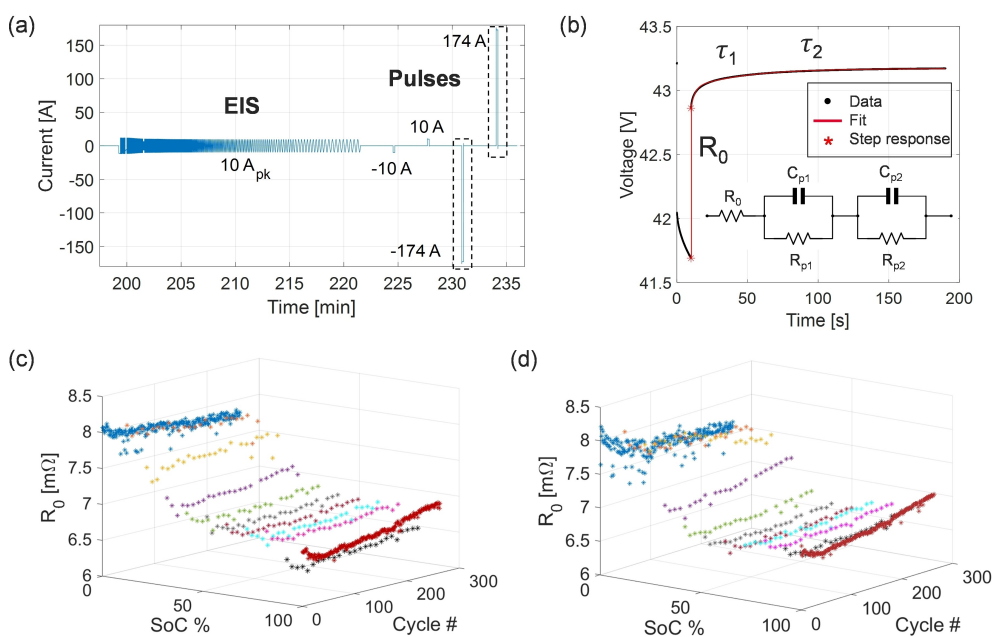

Figure 6. Extraction of ECM parameters from pulse response data. a) Current profile as a function of time for the EIS and pulse spot excitation tests at an SoC of 80%. The left dashed box shows the discharge pulse selected in panel (b). The duration of the pulses was $t = 10$ s. b) The voltage recovery phase (black, starting at $t = 10$ s) and the ECM fit (red), including the step response R_0 at $t = 10$ s and two RC elements ($R_{p1}||C_{p1}$; $R_{p2}||C_{p2}$) in series. c, d) The ECM fit parameter R_0 (ohmic resistance) shown in a 3D plot with respect to SoC and the cycle number, extracted from the -174 A discharge pulse (c), and from the 174 A charge pulse (d).

the pulse, and two RC elements in series describing the bi-exponential time-domain response (Figure 6b, inset). The median value of the root mean squared (RMS) error for the fitted EIS spectra was 56 μΩ, with higher values at low SoC. R_0 represents the cell constant and the electrolyte ionic resistance of the cells. The ohmic resistance R_0 has a clear dependency on the SoC as shown in Figures 6c and 6d for the two 174 A

pulses. R_0 starts at 8 mΩ at low SoCs and drops to 6.8 mΩ at high SoCs. R_0 shows a similar U-shape trend as $R_{sol} + R_{ct}$ in EIS with respect to SoC. The R_0 data generated from both the charging pulse (Figure 6c) and the discharging pulse (Figure 6d) are in good agreement over the different SoCs and the cycle number. In relation to the cycle number, R_0 shows an initial decrease followed by a slight increase, also similar to R_{sol}

$+R_{ct}$ in EIS. Quantitively, R_0 is slightly larger than R_{sol} from EIS, as it includes parts of the charge transfer resistance R_{ct}.[33] This is mostly because the pulse test data is sampled at 100 Hz, whereas R_{sol} from EIS is measured at around 200 Hz. After the initial step-function connected to R_0, the exponential voltage increase is described by two time constants τ_1 ($R_{p1}||C_{p1}$) and τ_2 ($R_{p2}||C_{p2}$). The faster time constant τ_1 is around one second and comprises both the double-layer capacitance and the charge transfer resistance due to the reactions at the electrode-electrolyte interface. The slower time constant τ_2 is around 20 seconds and it is related to slow ionic diffusion in the solid phase. Both time constants τ_1 and τ_2 were relatively constant over the 260 cycles. Similar values of the ECM fit parameters were obtained from the 10 A pulses; however, the signal-to-noise ratio of the voltage response data was slightly lower. Overall, these results show that while pulse measurements with short (3 minutes) recovery times can yield values for R_0 consistent with EIS data, longer recovery intervals may be necessary to accurately characterize τ_1 and τ_2 and detect their changes over time. In practice, the limited overall sampling time typically used in cycling studies will require a tradeoff between recovery interval length and elapsed cycles between consecutive measurements.

Conclusions and Outlook

A module test system was set up for testing a 7 kWh automotive battery module with 396 interconnected cells. An advanced calibration method was implemented for EIS, where the calibration accuracy was maintained by establishing a well-defined EIS calibration plane close to the module with minimum wire movements. Significant corrections on the resistance and the reactance were obtained from the calibration, particularly at high frequencies above 100 Hz. The module was charged and discharged up to 260 times, and after each cycle, spot measurements were done including an EIS sweep and time-domain pulses at different SoCs. From EIS data the main electrochemical parameters R_{sol}, R_{ct}, and L were robustly extracted. R_{sol} showed a decrease over the cycle numbers which is explained by the enhanced wetting of the electrodes due to new cells used in the module. R_{ct} showed a monotonic increase over the 260 cycles related to the module ageing, and the inductance L was constant at about 170 nH, as it is related to the module geometry, fixture and cables. From the pulse response the main time-domain parameters R_0, τ_1, and τ_2 were robustly extracted. R_0 showed a similar trend as $R_{sol}+R_{ct}$ over SoC and the cycle number. By adapting the pulse length and considering a longer pulse recovery time the ECM predict that the contribution of R_{ct} can be varied and R_0 can be moved closer to R_{sol}. In this work, a certain tradeoff between the overall sampling time and the number of cycles was considered, as well as the time constraints required for upcoming implementation in EV battery management systems. It is notable that we fit the EIS model with a single ZARC and the pulse data with two RC elements. The first RC element corresponds to the main EIS ZARC, while the second RC element, at a time constant of

about 20 seconds, corresponds well to the linear EIS Warburg tail which is around 50 mHz. Future studies will focus on advanced time-domain pulsing with longer pulse rest durations and electrochemical model interpretation and battery ageing, including also defined automotive test profiles following protocols like WLTP.

Conflict of Interest

The authors declare no conflict of interest.

Data Availability Statement

The data that support the findings of this study are available from the corresponding author upon reasonable request.

Keywords: battery module · electrochemical impedance spectroscopy · equivalent circuit model · impedance calibration · lithium-ion battery · time domain pulse test

[1] a) L. Zhu, F. Xiong, H. Chen, D. Wei, G. Li, C. Ouyang, *Int. J. Heat Mass Transfer* **2020**, *163*, 120384; b) M. Fichtner, *Batteries & Supercaps* **2022**, *5*, e202100224.

[2] a) M. F. R. Zwicker, M. Moghadam, W. Zhang, C. V. Nielsen, *J. of Adv. Joining Processes* **2020**, *1*, 100017; b) C. Yuan, Y. Deng, T. Li, F. Yang, *CIRP Ann.* **2017**, *66*, 53–56.

[3] S. Arora, A. Kapoor, *Batteries* **2019**, *5*, 70.

[4] S. Castano-Solis, D. Serrano-Jimenez, J. Fraile-Ardanuy, J. Sanz-Feito, *Electr. Power Syst. Res.* **2019**, *166*, 9–17.

[5] W.-J Zhang, *J. Power Sources* **2011**, *196*, 2962–2970.

[6] K. W. Beard, *Linden's Handbook of Batteries*, 5th edition, McGraw-Hill Education, **2019**.

[7] T. Osaka, D. Mukoyama, H. Nara, *J. Electrochem. Soc.* **2015**, *162*, A2529–A2537.

[8] A. Lasia, *Electrochemical Impedance Spectroscopy and Its Applications*, Springer-Verlag: New York **2014**, ISBN: 978–1-4614-8932-0.

[9] Q.-A Huang, Y. Shen, Y. Huang, L. Zhang, J. Zhang, *Electrochim. Acta* **2016**, *219*, 751–765.

[10] a) X. Kong, G. L. Plett, M. S. Trimboli, Z. Zhang, D. Qiao, T. Zhao, Y. Zheng, *J. Energy Storage* **2020**, *167*, 013539; b) N. Al-Zubaidi R-Smith, M. Kasper, P. Kumar, D. Nilsson, B. Mårlid, F. Kienberger, *Batteries* **2022**, *8*, 50.

[11] a) A. L. Rue, P. J. Weddle, R. J. Kee, T. L. Vincent, *American Control Conference (ACC)*, **2020**, 231–236; b) M. Berecibar, I. Gandiaga, I. Villarreal, N. Omar, J. Van Mierlo, P. V. -Bossche, *Renewable Sustainable Energy Rev.* **2016**, *56*, 572–587.

[12] X. Wang, X. Wei, Q. Chen, J. Zhu, H. Dai, *J. Energy Storage* **2019**, *26*, 100952.

[13] J. Jiang, Z. Lin, Q. Ju, Z. Ma, C. Zheng, Z. Wang, *Energy Procedia* **2017**, *105*, 844–849.

[14] T. Yokoshima, D. Mukoyama, H. Nara, S. Maeda, K. Nakazawa, T. Momma, T. Osaka, *Electrochim. Acta* **2017**, *246*, 800–811.

[15] N. Meddings, M. Heinrich, F. Overney, J.-S. Lee, V. Ruiz, E. Napolitano, S. Seitz, G. Hinds, R. Raccichini, M. Gaberšček, J. Park, *J. Power Sources* **2020**, *480*, 228742.

[16] M. Kasper, A. Leike, J. Thielmann, C. Winkler, N. Al-Zubaidi R-Smith, F. Kienberger, *J. Power Sources* **2022**, *536*, 231407.

[17] Z. Li, X. Shi, M. Shi, C. Wei, F. Di, H. Sun, *Asia Energy Elect. Engineering Symp. (AEEES)* **2020**, 753–757.

[18] J. P. Christophersen, *Battery Test Manual for Electric Vehicles, Revision 3*; United States: N. p., **2015**.

[19] A. S. Keefe, S. Buteau, I. G. Hill, J. R. Dahn, *J. Electrochem. Soc.* **2019**, *166*, A3272.

[20] U. Krewer, F. Röder, E. Harinath, R. D. Braatz, B. Bedürftig, R. Findeisen, *J. Electrochem. Soc.* **2018**, *165*, A3656.

[21] N. Al-Zubaidi R-Smith, M. Ragulskis, M. Kasper, S. Wagner, J. Pumsleitner, B. Zollo, A. Groebmeyer, F. Kienberger, *IEEE Trans. Instrum. Meas.* **2021**, *70*, 1–9.

[22] a) Z. Wang, G. Feng, D. Zhen, F. Gu, A. Ball, *Energy Reports* **2021**, *7*, 5141–5161; b) W. Waag, *Appl. Energy* **2013**, *102*, 885–897.

[23] I. Babaeiyazdi, A. Rezaei-Zare, S. Shokrzadeh, *Energy* **2021**, *223*, 120116.

[24] N. Al-Zubaidi R-Smith, M. Leitner, I. Alic, D. Toth, M. Kasper, M. Romio, Y. Surace, M. Jahn, F. Kienberger, A. Ebner, G. Gramse, *J. Power Sources* **2021**, *512*, 230459.

[25] P. M. Biesheuvel, Y. Fu, M. Z. Bazant, *Phys. Rev. E* **2011**, *83*, 061507.

[26] R. Xiong, Y. Pan, W. Shen, H. Li, F. Sun, *Renewable Sustainable Energy Rev.* **2020**, *131*, 110048.

[27] a) S. Buteau, J. R. Dahn, *J. Electrochem. Soc.* **2019**, *166*, A1611- A1622; b) H. Mu, R. Xiong, H. Zheng, Y. Chang, Z. Chen, H. Mu, *Appl. Energy* **2017**, *207*, 384–393.

[28] D. H. Jeon, *Energy Storage Mater.* **2019**, *18*, 139–147.

[29] M.-S. Wu, T.-L. Liao, Y.-Y. Wang, C.-C. Wan, *J. Appl. Electrochem.* **2004**, *34*, 797–805.

[30] F. J. Günter, J. B. Habedank, D. Schreiner, T. Neuwirth, R. Gilles, G. Reinhart, *J. Electrochem. Soc.* **2018**, *165*, A3249.

[31] a) J. Vetter, P. Novak, M. R. Wagner, C. Veit, K.-C. Möller, J. Besenhard, M. Winter, M. Wohlfahrt-Mehrens, C. Vogler, A. Hammouce, *J. Power Sources* **2005**, *147*, 269–281; b) X. Wang, X. Wei, H. Dai, *J. Energy Storage* **2019**, *21*, 618–631; c) Q. Zhang, X. Li, Z. Du, Q. Liao, *J. Energy Storage* **2021**, *40*, 102743.

[32] a) U. Tröltzsch, O. Kanoun, H.-R. Tränkler, *Electrochim. Acta* **2006**, *51*, 1664–1672; b) C. Pastor-Fernández, W. Dhammika Widanage, J. Marco, M.-Á. Gama-Valdez, Gael. H. Chouchelamane, *IEEE Trans. Electrification Conf. and Expo (ITEC)* **2016**, 1–6.

[33] A. Barai, K. Uddin, W. D. Widanage, A. McGordon, P. Jennings, *Sci. Rep.* **2018**, *8*, 21.